Nanotechnology 20 (2009) 175301 (11pp) doi:10.1088/0957-4484/20/17/175301

A control approach to high-speed probe-based nanofabrication

Yan Yan[1], **Qingze Zou**[1,3] **and Zhiqun Lin**[2]

[1] Department of Mechanical Engineering, Iowa State University, Ames, IA 50011, USA
[2] Department of Material Science and Engineering, Iowa State University, Ames, IA 50011, USA

E-mail: qzzou@iastate.edu

Received 7 January 2009, in final form 11 March 2009
Published 3 April 2009
Online at stacks.iop.org/Nano/20/175301

Abstract
In this paper, an inversion-based feedforward control approach for achieving high-speed, large-range probe-based nanofabrication is proposed. Probe-based nanofabrication has attracted great interest recently. This technique, however, is still limited by its low throughput, due to the challenges in compensating for the existing adverse effects. These adverse effects include the nonlinear hysteresis as well as the vibrational dynamics of piezoactuators used to position the probe in 3D axes, and the dynamic coupling in multi-axis motion during high-speed nanofabrication. The main contribution of this paper is the utilization of the recently developed model-less inversion-based iterative control technique to overcome these challenges in scanning probe microscope-based nanofabrication. By using this advanced control technique, precision position control of the probe can be achieved during high-speed, large-range multi-axis nanofabrication. The proposed approach is demonstrated in experiments by implementing it to fabricate large-size ($\sim$50 μm) pentagram patterns via mechanical scratching on a gold-coated silicon sample surface at high speed ($\sim$4.5 mm s^{-1}).

(Some figures in this article are in colour only in the electronic version)

1. Introduction

In this paper, an iterative feedforward control approach to achieve high speed and large range in probe-based nanofabrication is presented. Recently, probe-based nanofabrication using tools such as scanning probe microscopes (SPM) has attracted much interest. Current probe-based nanofabrication processes [1–5], however, are limited by the low throughput of the process, which, in turn, hinders their practical implementation. Although such a low throughput can be improved through hardware improvements such as parallel probes [5], the throughput is eventually limited if the fabrication is slow due to the hardware adverse effects [6]. During high-speed, large-range fabrication, hardware adverse effects can lead to large positioning errors of the probe relative to the sample, and as a result, large defects in the nanopatterns/parts fabricated. The contribution of this article is the implementation of a recently developed inversion-based iterative control approach [7] to compensate for the adverse hardware effects.

[3] Author to whom any correspondence should be addressed.

Precision positioning during high-speed, large-range motion is needed in probe-based nanofabrication. It has become evident that probe-based methods to fabricating nanoscale structures and devices are promising (because of their low cost and significant technical potential) [8]. Various nanofabrication processes have been proposed [1–5, 9]. All of these processes require the precision positioning of the probe relative to the sample, and thereby, are confronted by the same challenge—maintaining precision (probe-to-sample) positioning during high-speed, large-range operation. Large positioning errors can be generated during high-speed, large-range fabrication, which will not only lead to large defects in the fabricated structures or devices, but also result in damage of the probe (when the sample is hard), the sample (when the sample is soft), or both. Moreover, unlike other probe-based applications (such as SPM imaging) where the motion in one axis is substantially slower than that in other axes, the motion control in probe-based nanofabrication can be very demanding in all 3D axes. As a result, positioning errors in different axes can be superimposed and lead to large distortions in the final structure/device fabricated. Additionally, when the fabrication speed is high and/or the operation range is large, the cross-axis dynamics coupling of piezoactuators [10] can become large, resulting in large fabrication distortions as well. Therefore, it is important to maintain the precision positioning of the probe relative to the sample in all x–y–z axes during high-speed, large-size nanofabrication.

Advanced control techniques can be used to improve positioning precision during high-speed, large-range motion. For example, it has been demonstrated recently that the output tracking in repetitive operations can be substantially improved by using the inversion-based iterative control (IIC) techniques [10, 6, 11]. A main advantage of the iterative control approach is the exploitation of the noncausality gained from the repetitive nature of the applications, particularly for nonminimum-phase systems such as piezoactuators in SPM [12]. Also, it has been shown recently that the IIC approach can compensate for both hysteresis and dynamics effects of piezoactuators [6]. The model-less iterative control (MIIC) employed in this paper further extends the IIC approach [10], by eliminating the need for the dynamics modeling process in the control algorithm. Therefore, constraints related to the modeling process and the model accuracy are removed. The efficacy of the MIIC algorithm for precision positioning has been demonstrated through experiments [7, 13]. Specifically, we note that in nanofabrication, the desired trajectory is usually specified *a priori*, and the environment tends to be well maintained. Therefore, it is advantageous to utilize iterative control techniques such as MIIC in probe-based nanofabrication.

The main contribution of the paper is the use of the MIIC technique to probe-based nanofabrication using SPM. Particularly, the MIIC technique is utilized to compensate for the dynamics coupling effect in multi-axis motions, as well as to account for the hysteresis and the dynamics effects in the motion of each individual x, y and z axis. The approach is illustrated by implementing it to mechanically scratch a challenging pattern (pentagram) on a gold-coated silicon sample surface. The experimental results show that even at a fabrication speed as high as 4.5 mm s^{-1}, a large-size pentagram pattern ($\sim$50 μm by $\sim$50 μm) can still be accurately fabricated by using the proposed approach. Furthermore, a dashed-line pentagram pattern was also fabricated, and the experimental results obtained demonstrate the efficacy of the proposed method for high-speed 3D nanofabrication.

2. MIIC approach to probe-based nanofabrication

In this section, the use of the MIIC technique [7] in probe-based nanofabrication is presented. We start with briefly describing the probe-based nanofabrication process.

2.1. Probe-based nanofabrication

In probe-based nanofabrication, a micro-machined probe is precisely positioned on (or closely above) the same surface during the motion (see figure 1) to locally induce surface modification along the path, resulting in nanoscale features on the sample surface (such as lines or dots). Such a

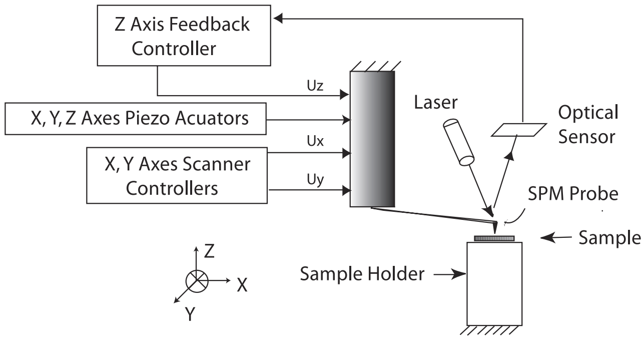

Figure 1. The schematic diagram of the SPM system.

surface modification can be achieved, for example, through mechanical scratching followed by an etching process [2, 3], or, through thermal effects as exemplified in the IBM Millipede system [5]. Alternatively, probe-based nanofabrication can also be achieved by introducing external effects such as electrical fields [1], laser beams [9], and chemical compounds (via probe coating) [4]. In all these mechanisms, maintaining the probe-to-sample positioning precision is critical, because the probe-to-sample positioning error is directly translated to defects in the fabricated nanostructures/devices. The probe–sample precision positioning becomes challenging when the nanofabrication is at high speed and large range, due to the excitation of adverse effects including the cross-axis dynamics coupling, the hysteresis, as well as the vibrational dynamics effects [6, 10, 14].

2.2. MIIC approach to multi-axis motion control

We propose to utilize the recently developed MIIC approach [7] to compensate for the above adverse effects during probe-based nanofabrication. The iterative learning control (ILC) approach is attractive because in nanofabrication, the desired trajectories for all x–y–z axes are usually pre-specified and repetitive. Therefore, it is possible to utilize the entire trajectory tracking from the previous iteration to generate the control input at the current time instant. In other words, the ILC approach provides the possibility to explore the noncausality in nanofabrication to enhance the precision positioning.

The MIIC algorithm is described in the frequency domain as

$$\begin{aligned} u_0(\mathrm{j}\omega) &= \alpha y_\mathrm{d}(\mathrm{j}\omega) \\ u_{k+1}(\mathrm{j}\omega) &= \frac{u_k(\mathrm{j}\omega)}{y_k(\mathrm{j}\omega)} y_\mathrm{d}(\mathrm{j}\omega), \\ &(\text{for } u_k(\mathrm{j}\omega) \neq 0,\ y_k(\mathrm{j}\omega) \neq 0,\ k \geqslant 1) \end{aligned} \tag{1}$$

where $\alpha \neq 0$ is a pre-chosen constant (e.g., α can be chosen as the estimated DC-gain of the system dynamics), $f(\mathrm{j}\omega)$ denotes the Fourier transform of the signal $f(t)$, $y_\mathrm{d}(\mathrm{j}\omega)$ is the desired output trajectory, and $u_k(\mathrm{j}\omega)$ and $y_k(\mathrm{j}\omega)$ are the input and the output obtained from the kth iteration, respectively (see figure 2).

The MIIC technique extends the inversion-based iterative control (IIC) technique proposed in [10]. The MIIC algorithm

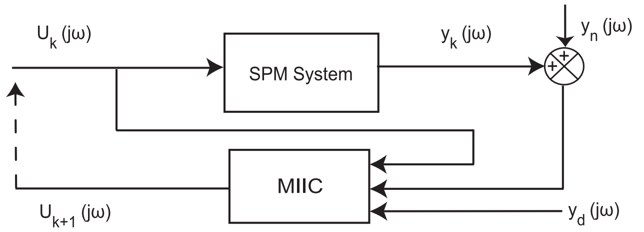

Figure 2. The block diagram of the MIIC algorithm.

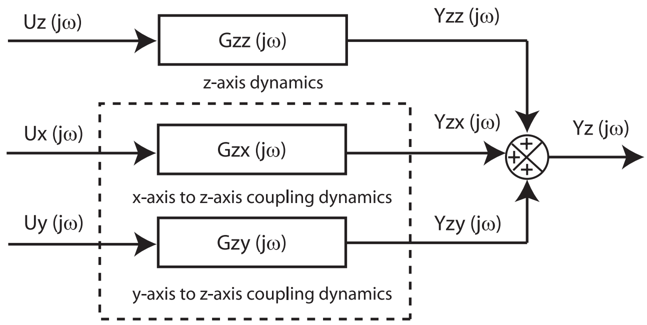

Figure 3. The z-axis AFM dynamics with x–y-to-z coupling effect.

(equation (1)) can be transformed from the IIC algorithm by replacing the inverse of the dynamics model, $G_{ff}^{-1}(\mathrm{j}\omega)$, in the IIC algorithm (see equation (9) in [10]) with $u_k(\mathrm{j}\omega)/y_k(\mathrm{j}\omega)$, and setting the iterative coefficient $\rho(\omega) = 1$. Such a transformation implies that the dynamics modeling process is eliminated in the MIIC algorithm, whereas the IIC algorithms require a reasonably good dynamics model of the system, and the convergence rate (i.e., the choice of the iterative coefficient) depends on the model accuracy. Thus, the MIIC technique alleviates these modeling-related constraints and can achieve better tracking performance, particularly when the desired output trajectory is complex [15].

We note that in nanofabrication, the existing disturbance and measurement noise effects need to be addressed. The disturbance/noise effects can be modeled as an extraneous random output augmented to the system output—with that, the output becomes $\hat{y}_k(\mathrm{j}\omega) = y_k(\mathrm{j}\omega) + y_n(\mathrm{j}\omega)$, where $y_k(\mathrm{j}\omega)$ denotes the linear part of the system response, i.e., $y_k(\mathrm{j}\omega) = G(\mathrm{j}\omega)u_k(\mathrm{j}\omega)$, and $y_n(\mathrm{j}\omega)$ denotes the noise/disturbance. Then it can be shown that if the bound of the following noise/disturbance to the desired signal ratio (NSR), $\epsilon(\omega)$, is less than $1-\sqrt{2}/2$, i.e., $\epsilon(\omega) \triangleq |y_n(\mathrm{j}\omega)|/|y_d(\mathrm{j}\omega)| \leqslant [1-\sqrt{2}/2]$, the output tracking can be improved by using the MIIC algorithm [7],

$$\lim_{k\to\infty}\left|\frac{y_k(\mathrm{j}\omega)-y_{\mathrm{d}}(\mathrm{j}\omega)}{y_{\mathrm{d}}(\mathrm{j}\omega)}\right| \leqslant \frac{2\epsilon(\omega)[1-\epsilon(\omega)]}{1-2\epsilon(\omega)} < 1. \tag{2}$$

The above equation (2) shows that precision tracking of the desired trajectory over a broad frequency range can be achieved provided that the NSR $\epsilon(\omega)$ is small (in that frequency range). The 'trackable' frequency range can be larger than the open-loop bandwidth of the system [7, 13].

2.3. Compensating for the cross-axis coupling effect using MIIC

Compensating for cross-axis dynamics coupling existing in multi-axis motion control [10, 16, 17] is particularly important when fabricating 3D nanodevices/patterns, because the motions in all x–y–z axes can be complicated and at high speed. Although the cross-axis coupling effects can be accounted for by considering the 3D (x–y–z axes) SPM dynamics as a multi-input-multi-output (MIMO) system, and then designing a MIMO controller accordingly [18], such an approach involves complicated online computations, and its performance can be hampered by the possibly large model uncertainties. In this paper, the MIIC algorithm (equation (1)) is used to compensate for, not only the dynamics and hysteresis effects in each axis [7], but also the cross-axis dynamics coupling effects. Such a cross-axis coupling is pronounced from the large-range lateral x–y axes motion to the vertical z-axis motion, and becomes more significant in high-speed operation. As schematically shown in figure 3, the x–y-to-z coupling-caused displacement $y_{zxy}(\mathrm{j}\omega)$ is augmented to the displacement of the z-axis itself $y_{zz}(\mathrm{j}\omega)$, leading to the total z-axis displacement $y_z(\mathrm{j}\omega)$ as,

$$\begin{aligned} y_z(\mathrm{j}\omega) &= G_{zz}(\mathrm{j}\omega)u_z(\mathrm{j}\omega) + G_{zx}(\mathrm{j}\omega)u_x(\mathrm{j}\omega) + G_{zy}u_y(\mathrm{j}\omega) \\ &\triangleq y_{zz}(\mathrm{j}\omega) + y_{zxy}(\mathrm{j}\omega). \\ &(y_{zxy}(\mathrm{j}\omega) \triangleq G_{zx}(\mathrm{j}\omega)u_x(\mathrm{j}\omega) + G_{zy}(\mathrm{j}\omega)u_y(\mathrm{j}\omega)). \end{aligned} \tag{3}$$

Thus first, the x–y-to-z coupling-caused displacement $y_{zxy}(\mathrm{j}\omega)$ is measured by applying the control input to the lateral x–y axes on a hard flat reference sample (e.g., a silicon sample or a sapphire calibration sample). Then, the desired z-axis displacement $y_{z,\mathrm{d}}(\mathrm{j}\omega)$ is modified by subtracting the measured coupling-caused displacement $y_{zxy}(\mathrm{j}\omega)$,

$$\hat{y}_{z,\mathrm{d}}(\mathrm{j}\omega) = y_{z,\mathrm{d}}(\mathrm{j}\omega) - y_{zxy}(\mathrm{j}\omega), \tag{4}$$

and the MIIC technique is applied to the z-axis only (with no lateral displacement, i.e., $y_{zxy}(\mathrm{j}\omega) = 0$ in (4)) to find the control input $u_z^*(\mathrm{j}\omega)$ that tracks the modified z-axis desired trajectory, i.e.,

$$G_{zz}(\mathrm{j}\omega)u_z^*(\mathrm{j}\omega) = y_{zz}(\mathrm{j}\omega) \longrightarrow \hat{y}_{z,\mathrm{d}}(\mathrm{j}\omega). \tag{5}$$

Finally, the control inputs for both the lateral x–y and z-axis tracking are applied simultaneously during the fabrication. As a result, the x–y-to-z coupling is removed and precision positioning in all x–y–z axes is achieved. We note that a similar approach to compensate for the cross-axis coupling has been proposed in [10]. The above method extends the work in [10] for nanofabrication by achieving precision trajectory tracking in all three x–y–z axes at the same time.

3. Experimental example

We illustrate the MIIC approach to probe-based nanofabrication through experiments. It is demonstrated that by using the MIIC approach, high-speed nanofabrication of a challenging pattern (pentagram) of large size can be achieved. We start with briefly describing the nanofabrication process based on mechanical scratching.

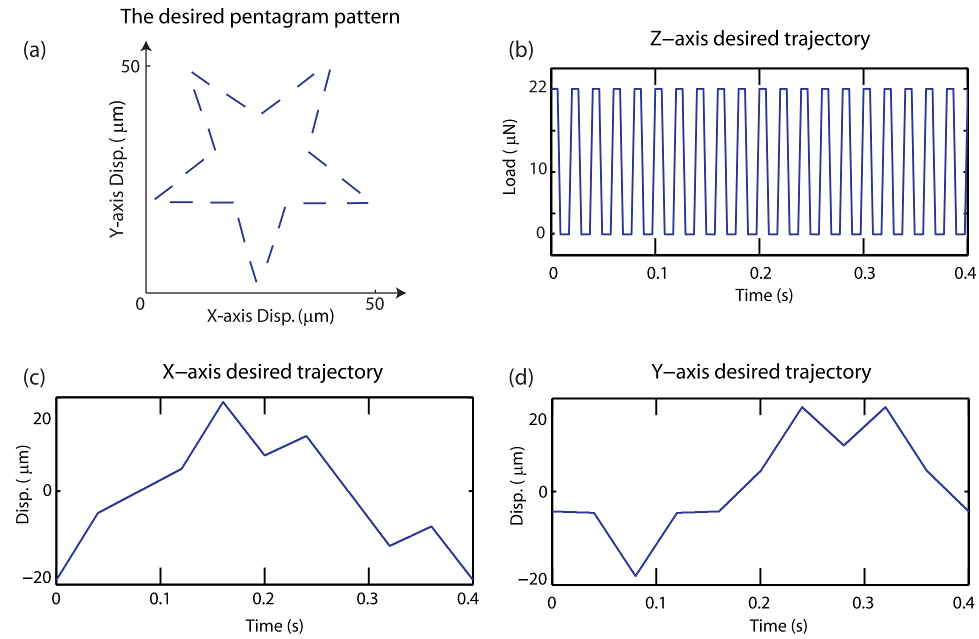

Figure 4. The desired trajectories of the dash-line pentagram pattern: (a) the entire trajectory, (b) the z-axis trajectory, (c) the x-axis trajectory, and (d) the y-axis trajectory.

3.1. Nanofabrication based on mechanical scratching

The experiments were carried out under ambient conditions on a SPM system (Dimension 3100, Veeco Instruments Inc.) with a rectangular-shape cantilever coated with wear-resistant material. The nominal stiffness of the probe is 40 N m^{-1} (stiffer probes like the stainless steel cantilever with diamond tip can be used to further reduce wear and increase the smoothness of the fabricated pattern). By applying a relatively large loading force to the SPM probe on the sample surface, and dragging the probe to track the desired geometry path, patterns of nanoscale features can be fabricated. The fabricated pattern can be examined by imaging the sample surface using the same SPM system with a substantially lower loading force. In applications, the mechanical-scratching method is usually used to fabricate fine patterns on a soft metal or polymer material such as PMMA [19]. For harder material such as silicon, the mechanical-scratching technique has been successfully used to fabricate multilayer nanometer devices along with an etching process [20]. We note that as discussed before, the precision positioning problem ubiquitously exists in probe-based nanofabrication processes. Therefore, we expect that the proposed MIIC technique can be equally applied to other probe-based nanofabrication processes as well.

3.2. Experimental setup

The SPM system utilized in this paper uses piezotube actuators to position the SPM probe with respect to the sample in all x–y–z axes. All the control inputs were generated by using MATLAB-xPC-target (Mathworks, Inc.), and sent through a data acquisition card to drive the high-voltage amplifiers for the corresponding piezotube actuators.

In the following experiments, two types of pentagram (one with continuous lines, and the other with dashed lines) were chosen as the desired patterns to be fabricated. When fabricating the continuous-line pentagram pattern, contact mode SPM was used to maintain the cantilever deflection around a setpoint value (i.e., to maintain a constant tip–sample interaction force) by using the feedback controller of the SPM system for the z-axis probe positioning. When fabricating the dashed-line pentagram pattern, the z-axis feedback control was turned off, and the vertical position of the z-axis piezoactuator was controlled by applying the feedforward input obtained from the MIIC technique to track the desired z-axis trajectory. The fabrication of the dashed-line pentagram pattern required the up-and-down vertical motion of the probe. Thus, such an experiment evaluated the MIIC algorithm for fabricating 3D structures. The desired pentagram pattern (size: $\sim$50 μm by $\sim$50 μm) and the corresponding desired trajectories for each z, x, and y axis are shown in figures 4(a), (b), (c), and (d), respectively. Particularly, an isosceles trapezoidal wave was chosen as the desired z-axis waveform. The use of the isosceles trapezoidal wave rather than square wave was to reduce the oscillations after the up–down transitions. The entire pentagram pattern comprised a total of 20 dash lines evenly spaced (figure 4(b)).

3.3. SPM dynamics

The SPM dynamics in each axis (x, y, and z) was measured experimentally. For example, the lateral x-axis dynamics from the input voltage to the displacement output of the piezotube actuator was measured using a dynamic signal analyzer (DSA, Hewlett Packard 356653A). Also, the dynamics uncertainty was experimentally quantified by measuring the frequency responses under different driven input levels (20, 40, and 60 mV), as shown in figure 5 for the frequency range $\omega \in [0, 3]$ kHz. When measuring the z-axis SPM dynamics

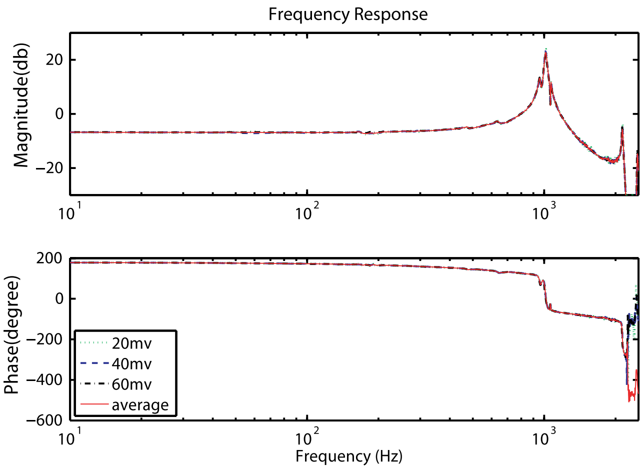

Figure 5. The frequency responses of the x-axis piezoelectric actuator on the SPM, measured with three different input amplitude levels (20, 40, and 60 mV), with comparison to the averaged response.

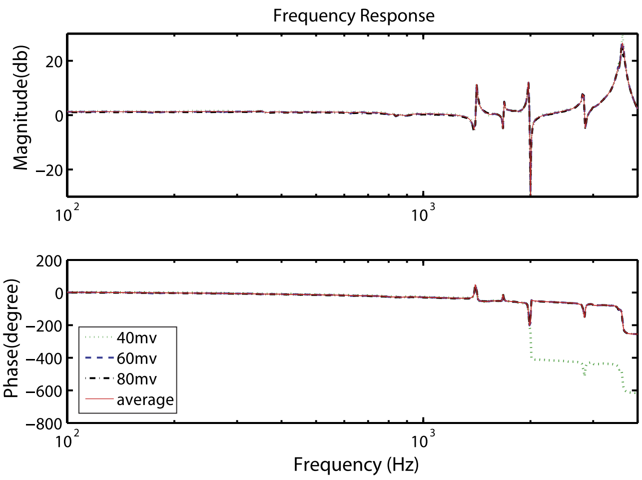

Figure 6. The frequency responses of the z-axis piezoelectric actuator on the SPM, measured with three different input amplitude levels (40, 60, and 80 mV), with comparison to the averaged response.

(from the input voltage of the z-axis piezoactuator to the cantilever deflection), the cantilever probe was pressed onto a hard silicon sample with a preload constant force and a sinusoidal oscillatory force of small amplitude was applied with the sinusoidal frequency sweeping over the measured range (i.e., the swept-sine method). Therefore, the obtained frequency response should mainly contain the dynamics of the piezoelectric actuator and the cantilever along with the mechanical fixture connecting them (as the surface is hard). The measured frequency response is shown in figure 6 for the frequency range $\omega \in [0, 4]$ kHz. We note that the implementation of the MIIC algorithm did not require an *a priori* dynamics modeling process (see equation (1)). Instead, the SPM dynamics in figures 5 and 6 were measured to evaluate the performance of the proposed MIIC technique for high-speed nanofabrication.

3.4. Tracking results and discussion

In the experiments, the MIIC technique was applied to achieve precision tracking in all x–y–z axes simultaneously (as described in section 2), and then, the converged inputs were used to fabricate the pattern by applying a large load force ($\sim$22 μN) to the cantilever. For comparison, we also used the DC-gain method to fabricate the pentagram pattern, where the control input was generated by scaling the desired output with the DC-gain of the piezoactuator. The DC-gain method does not account for the hysteresis nor the vibrational dynamics effects, thereby the fabricated patterns demonstrated these adverse effects on the fabrication quality.

To compensate for the x–y-to-z coupling effect, the coupling-caused z-axis displacement was measured from the cantilever deflection (in vertical direction) when pressing the probe onto a hard silicon sample of nanoscale flatness (the surface roughness was within a couple of nanometers) and applying the x-axis and y-axis control inputs to track the x, y-axis desired trajectories, respectively (see figures 4(c) and (d)). Then the modified z-axis desired trajectory was obtained as described in section 2.3, and the MIIC algorithm was used to obtain the control input to track this modified z-axis desired trajectory. Finally, this control input was applied to the z-axis when the control inputs to the other two axes were applied, simultaneously. We note that for this SPM system, other cross-axis coupling effects including vertical to lateral and between lateral x–y axes were small and negligible.

The experimental tracking results in all x–y–z axes were acquired and compared. Three different fabrication rates (5, 15 and 25 Hz) were tested in the experiment, where the fabrication rate was defined as the rate to finish the fabrication of the entire pattern once. The corresponding average lateral speeds for the three fabrication rates were at $\sim$0.9 mm s^{-1}, $\sim$2.7 mm s^{-1}, and $\sim$4.5 mm s^{-1}, respectively. At these three fabrication rates, the corresponding z-axis waveform frequency (for fabricating the dashed-line pentagram pattern) was 100, 300, and 500 Hz, respectively. In figure 7, the lateral x-axis tracking results for the fabrication rates of 5 and 25 Hz obtained by using the converged MIIC inputs are compared with the desired trajectory as well as those obtained by using the DC-gain method. To evaluate the z-axis tracking (with no lateral x–y axes displacement), the modified desired trajectory was used (to account for the x–y-to-z coupling) when the MIIC was applied, and the original desired trajectory was used when the DC-gain method was applied. The tracking results for the waveform frequencies of 100 Hz and 500 Hz (corresponding to the fabrication rates of 5 Hz and 25 Hz, respectively) are shown in figure 8 for the MIIC method and figure 9 for the DC-gain method. During the implementation of the MIIC technique, the iterations were stopped when the tracking error cannot be further reduced. Finally, the z-axis tracking during the fabrication process (i.e., when all x–y–z axes inputs were applied simultaneously) was also compared for the MIIC method and the DC-gain method with respect to the original z-axis desired trajectory, as shown in figure 10.

The tracking performance was also evaluated by quantifying the relative RMS tracking error and the relative

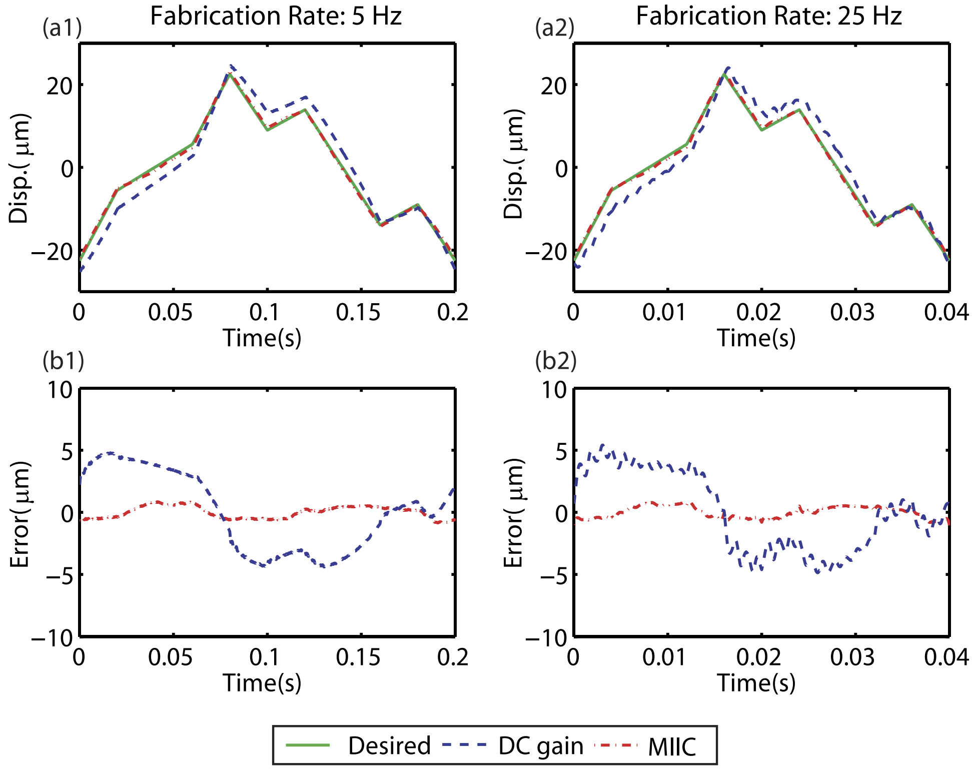

Figure 7. Comparison of the lateral x tracking results obtained by using the MIIC technique with those by using the DC-gain method at (a1) 5 Hz and (a2) 25 Hz, and comparison of the corresponding tracking errors at (b1) 5 Hz and (b2) 25 Hz, respectively.

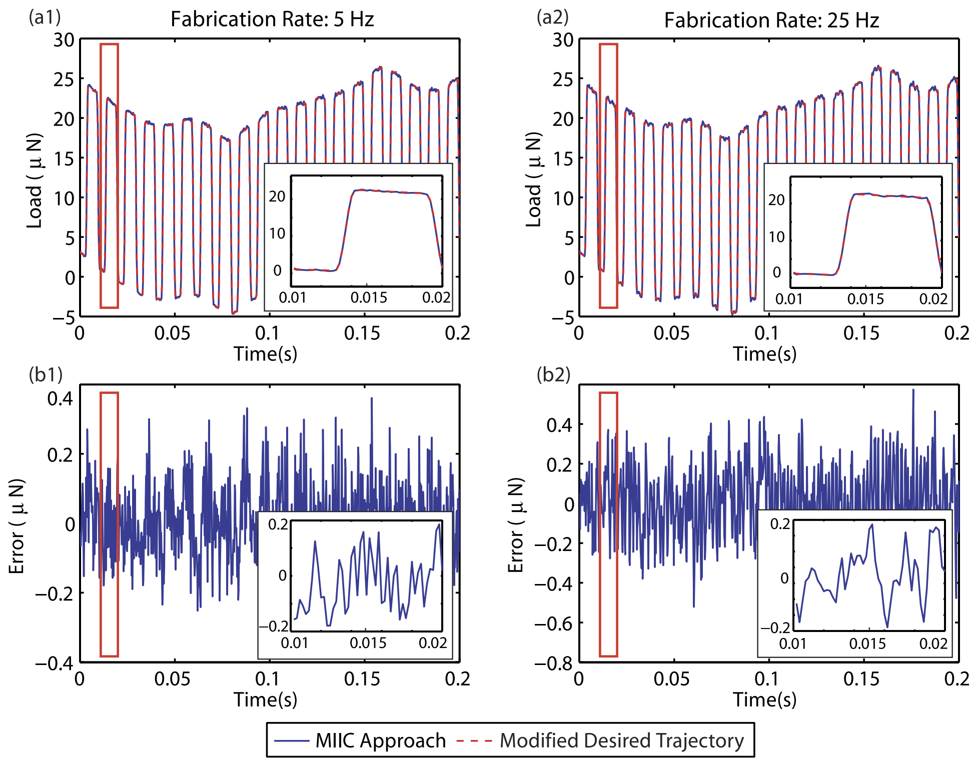

Figure 8. Comparison of the vertical z tracking results by using the MIIC technique with the modified desired trajectory at (a1) 5 Hz, (a2) 25 Hz, and comparison of the corresponding tracking errors at 5 Hz (b1), (b2) 25 Hz, respectively, where the insets are the zoomed-in view of ((a1), (a2)) the tracking and ((b1), (b2)) the tracking error in the second period (marked by a rectangle on the left).

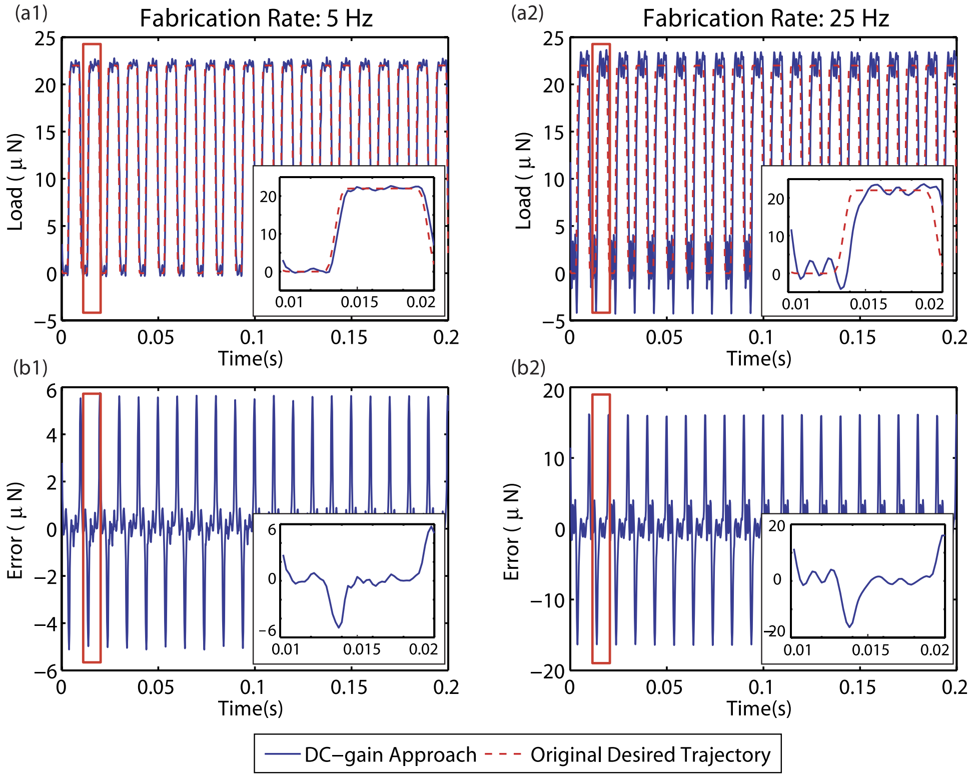

Figure 9. Comparison of the vertical z tracking results by using the DC-gain method with the original desired trajectory at (a1) 5 Hz, (a2) 25 Hz, and comparison of the corresponding tracking errors at (b1) 5 Hz, (b2) 25 Hz, respectively, where the insets are the zoomed-in view of ((a1), (a2)) the tracking and ((b1), (b2)) the tracking error in the second period (marked by a rectangle box to the left).

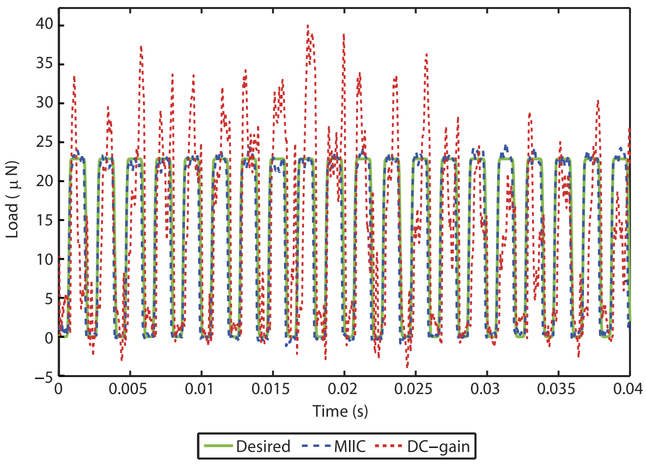

Figure 10. Comparison of the z-axis deflection signal by using the MIIC technique with that by using the DC-gain method at 25 Hz during the fabrication process (i.e., when the lateral x–y axes inputs were also applied simultaneously).

maximum tracking error, as listed in table 1 for the lateral tracking and table 2 for the vertical tracking, where the relative maximum tracking error $E_{\mathrm{M}}(\%)$, and the relative RMS tracking error $E_{\mathrm{RMS}}(\%)$ are defined as

$$E_{\mathrm{M}}(\%) \triangleq \frac{\|y_d(\cdot) - y_k(\cdot)\|_\infty}{\|y_d(\cdot)\|_\infty} \times 100\%,$$
$$E_{\mathrm{RMS}}(\%) \triangleq \frac{\|y_d(\cdot) - y_k(\cdot)\|_2}{\|y_d(\cdot)\|_2} \times 100\%. \tag{6}$$

Table 1. Comparison of the tracking errors in X-axis obtained by using the DC-gain method and the MIIC approach at different fabrication rates.

	Error					
	E_{M} (%)			E_{RMS} (%)		
Fab. rate (Hz)	5	15	25	5	15	25
Speed (mm s^{-1})	0.64	1.93	3.21	0.64	1.93	3.21
1st Iter.	3.81	3.67	4.23	1.49	1.39	1.41
2nd Iter.	2.04	2.12	2.11	1.15	1.12	1.20
3rd Iter.	1.80	1.90	2.44	1.09	1.05	1.13
4th Iter.	1.88	1.97	2.30	0.99	1.09	1.14
DC-gain	10.66	11.53	12.05	7.02	6.92	7.16

Table 2. Comparison of the tracking errors in Z-axis obtained by using the DC-gain method, and the MIIC approach at different fabrication rates.

	Error					
	E_{M} (%)			E_{RMS} (%)		
Fab. rate (Hz)	5	15	25	5	15	25
1st Iter.	5.18	5.84	7.57	0.78	0.86	1.80
2nd Iter.	2.03	2.30	3.28	0.55	0.64	0.87
3rd Iter.	1.14	1.20	2.06	0.34	0.44	0.50
4th Iter.	1.16	1.18	2.21	0.34	0.43	0.57
DC-gain	26.15	52.81	74.82	9.07	18.48	28.31

3.4.1. Discussion. The experimental results demonstrate that precision positioning in lateral x–y axes motion can be achieved by using the MIIC algorithm during large-range, high-speed nanofabrication. As the lateral displacement range was large (50 μm), the hysteresis effect was pronounced, and large positioning errors were generated. As shown in figures 7(a1) and (b1), with the DC-gain method, the hysteresis-caused relative maximum error $E_M(\%)$ was over 10% of the total displacement range when the fabrication rate was slow (5 Hz). Such a large positioning error was substantially reduced by using the MIIC algorithm—the relative RMS error $E_{RMS}(\%)$ and the relative maximum error $E_M(\%)$ were reduced to 0.99% and 1.88%, respectively. As the fabrication rate was increased to 25 Hz, the vibrational dynamics effect was augmented to the hysteresis effect, resulting in even larger tracking errors. However, precision tracking was still maintained when using the MIIC approach— $E_{RMS}(\%)$ and $E_M(\%)$ were only 1.14% and 2.30%, respectively (see figures 7(a2), (b2) and table 1). We note that for nanofabrication application, precision tracking in x and y axes are equally crucial, because even if the tracking error in each individual axis is small, a relatively large distortion can still be generated in the final fabricated pattern. Such an 'amplification' of the positioning error is caused by the superposition of the errors in different axes. In the experiment, precision tracking in y axis was also achieved by using the MIIC technique. The simultaneous precision tracking in both x and y axes led to the precision fabrication of the continuous-line pentagram pattern.

When fabricating the dashed-line pentagram pattern, the frequency of the isosceles trapezoidal wave was much higher (20 times higher) than that in the lateral x–y axes. As a result, large probe oscillations in the vertical z-axis not only increased the roughness of the sample surface, but can also further damage the probe, the sample, or both. By using the MIIC algorithm, however, even at the fabrication rate of 25 Hz, precision vertical z-axis tracking was still achieved—the $E_{RMS}(\%)$ was only 2% of that by using the DC-gain method (see figures 8 and 9 and table 2). Thus, the MIIC algorithm can effectively account for adverse effects during high-speed, large-size nanofabrication in both lateral and vertical directions.

The experimental results also showed that coupling-caused disturbance in multi-axis motion can also be effectively removed by using the proposed method (see section 2.3). Comparing the modified z-axis desired trajectory (in figure 8) with the original one (in figure 9), we can see that the x–y-to-z coupling effect was substantial. The coupling-caused z-axis displacement was ~40% of the (original) desired trajectory when the lateral x–y axes displacement was large (50 μm) and the velocity was at high speed (4.5 mm s^{-1}). Such a large coupling-caused disturbance was augmented to the vibrational dynamics effect when all 3D inputs were applied simultaneously during the nanofabrication of the dashed-line pentagram, resulting in much larger tracking error (than that if there were no coupling effect). This is evident by comparing with the DC-gain tracking result in figure 9. In contrast, such a large coupling-caused disturbance was removed with the use of the proposed MIIC technique, and precision tracking of the original z-axis desired trajectory was achieved during the 3D nanofabrication. Note that in figure 10, the small oscillations at the top and the bottom of the isosceles waves were generated because the SPM cantilever needed to be pulled out and pushed onto the sample surface during the fabrication. Therefore, the experimental results demonstrate that the proposed approach can achieve high-speed precision positioning in 3D probe-based nanofabrication at large size.

3.5. Nanofabrication results and discussion

3.5.1. Nanofabrication of continuous-line pentagram pattern. Next, to fabricate the continuous-line pentagram pattern, the MIIC inputs were applied to the x and y axes simultaneously with a larger load force. Then the fabricated sample area was imaged immediately afterward on the same SPM system. The SPM images of the fabricated patterns obtained by using the MIIC technique are compared with those obtained by using the DC-gain method in figure 11 for the three fabrication rates (5, 15 and 25 Hz). For comparison, the desired pentagram pattern was also marked by the blue-dashed line in figure 11. As shown in figure 11, the MIIC technique effectively removed the fabrication distortion caused by the hysteresis and the vibrational dynamics effects. When the fabrication speed was relatively slow at 5 Hz (the corresponding averaged line speed was ~0.9 mm s^{-1}, see figure 11(a1)), the distortion in the fabricated pattern was already obvious. Such pronounced distortions were mainly caused by the nonlinear hysteresis effect existing in both x- and y-axes piezoactuators (because the fabrication size was large, 50 μm). Particularly, the positioning errors were amplified due to the superimposition of the x-axis errors with the y-axis ones, caused mainly by the phase-delay and asynchronization between the x and the y axes. In contrast, the use of the MIIC approach effectively removed such fabrication distortions (see figure 11(b1)). When the fabrication rate was increased to 15 Hz (the corresponding average line speed was ~2.7 mm s^{-1}), the tracking error caused by the vibrational dynamics became significant, resulting in large oscillatory distortions in the fabricated pattern when the DC-gain method was used (see figure 11(a2)), which became even larger when the fabrication rate was further increased to 25 Hz (the average line speed was at 4.5 mm s^{-1}, see figure 11(a3)). Using the MIIC technique, precision tracking was still maintained during this high-speed, large-range fabrication. As shown in figure 11(b2) and (b3), the pattern distortion was very small, and the fabricated pattern almost overlapped with the desired one (marked by the blue-dashed line in figure 11). Therefore, the experimental results demonstrate that by using the MIIC approach, high-speed probe-based nanofabrication of a 2D pattern can be achieved.

3.5.2. Nanofabrication of the dashed-line pentagram pattern. Next, the converged MIIC inputs for all the x–y–z axes were applied to the x, y, and z axes respectively at the same time (the z-axis feedback control was turned off), and the dashed-line pentagram pattern was fabricated. Then the fabricated sample area was imaged immediately afterward on the same SPM. The SPM images of the fabricated patterns obtained by

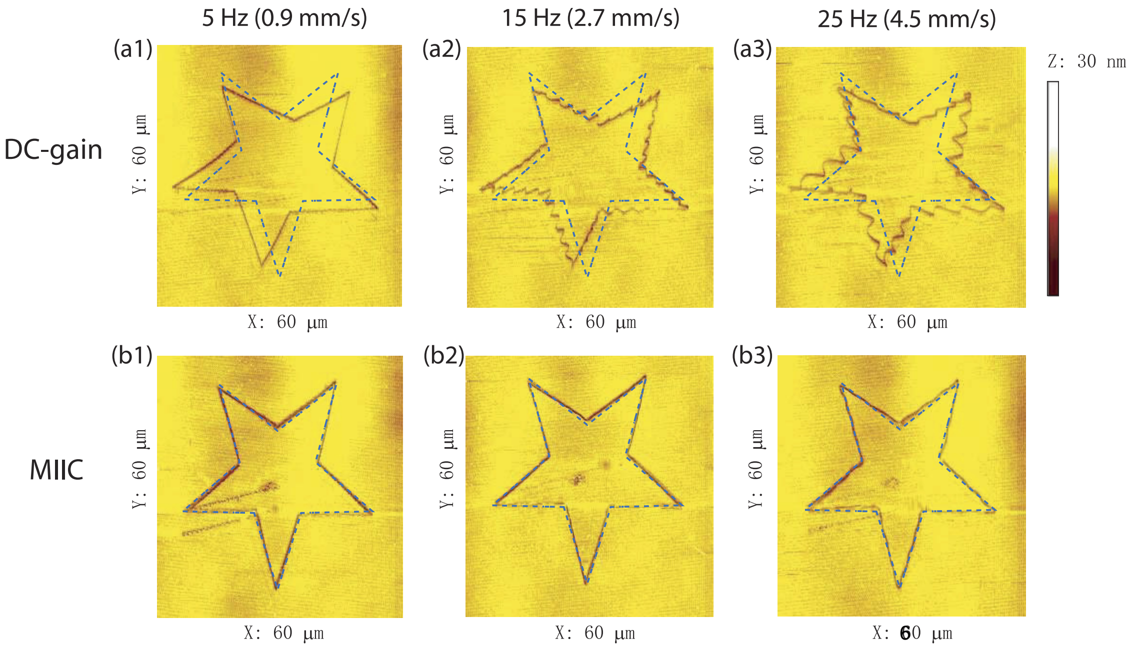

Figure 11. Comparison of the nanofabrication images of the continuous pentagram pattern obtained by using (top row) the DC-gain method with (bottom row) those obtained by using the MIIC technique at ((a1), (b1)) 5 Hz, ((a2), (b2)) 15 Hz, and ((a3), (b3)) 25 Hz, respectively, where the corresponding average line speeds are given in the title, and the blue-dashed lines represent the desired pentagram pattern.

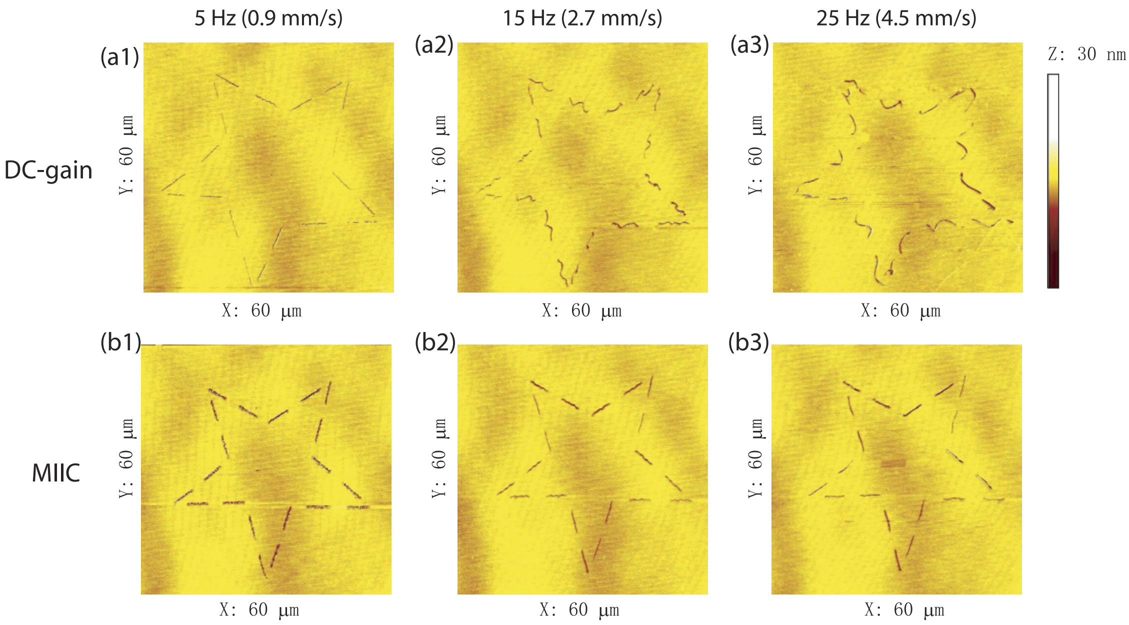

Figure 12. Comparison of the nanofabrication images of the dashed-line pentagram pattern obtained by (top row) using the DC-gain method with (bottom row) those obtained by using the MIIC technique at ((a1), (b1)) 5 Hz, ((a2), (b2)) 15 Hz, and ((a3), (b3)) 25 Hz, respectively, where the corresponding average line speeds are given in the title.

using the MIIC technique are compared with those obtained by using the DC-gain method (applied to all 3D axes) in figure 12 for the three fabrication rates (5, 15 and 25 Hz). To avoid confusion, the desired pentagram pattern was not marked out in figure 12. We also examined the indentation depth of the dashed-line by the cross-section plot shown in figure 13—the indentation depth was ∼10 nm.

The experimental results demonstrated the efficacy of the proposed approach in achieving 3D precision positioning during high-speed probe-based nanofabrication. When the fabrication rate was at 5 Hz, the distortions caused by nonlinear hysteresis and vibrational dynamics effects were already pronounced. As shown in figure 12(a1), the dashed lines in the pattern obtained by using the DC-gain method were curved (rather than straight) and varied in length. However, such large fabrication errors in the dashed lines were significantly reduced by using the MIIC method: the dash lines were straight and uniform in length, close to the desired ones (see

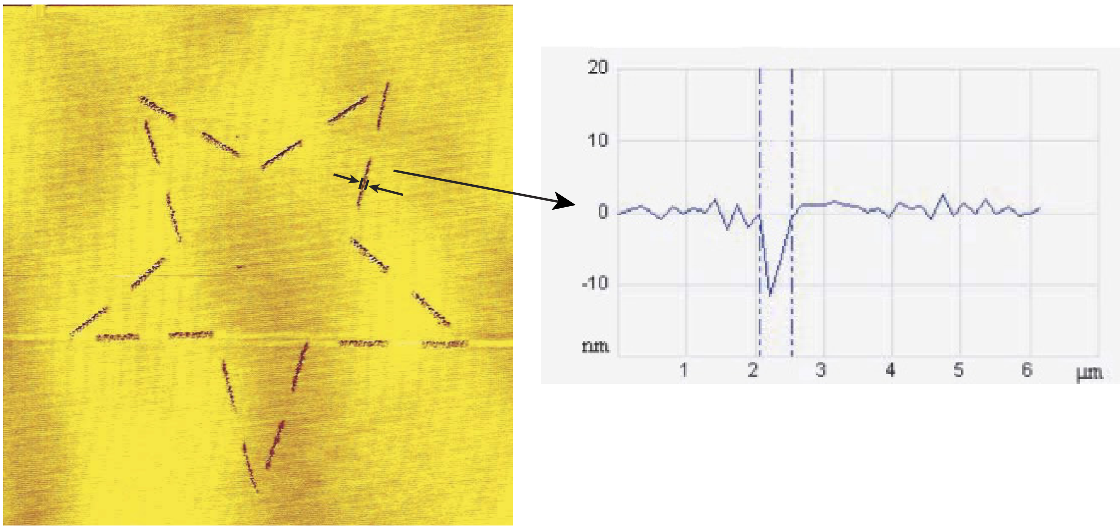

Figure 13. The cross-section image of the dashed pentagram. The right image shows the depth of the fabricated groove.

figures 12(b1) and 4(a)). When the rate was increased to 15 and 25 Hz, the hysteresis and dynamics caused pattern distortions became much more severe. As shown in figures 12(a2) and (a3), the dashed lines were more curved and varied greatly in length. In contrast, such large pattern distortions were substantially reduced by using the proposed method. As a result, the pentagram patterns were close to the desired one (see figures 12(b2) and (b3)). To the best knowledge of the authors, figures 11(b3) and 12(b3) represent one of the fastest probe-based nanofabrication results ever achieved (in terms of the line speeds in both the lateral and the vertical directions). Therefore, the experimental results demonstrated that the MIIC approach can be effectively utilized for high-speed nanofabrication of large-size 3D patterns.

4. Conclusion

A control approach to achieve probe-based high-speed nanofabrication at large range has been proposed. It was shown that the implementation of the MIIC technique to SPM probe-based nanofabrication can effectively compensate for the nonlinear hysteresis and vibrational dynamics effects of the piezotube actuator as well as the dynamic coupling effect, thereby improving the fabrication throughput. The approach has been illustrated by implementing it to fabricate a pentagram via mechanical scratching on a gold-coated silicon sample surface. The experimental results showed that pentagram patterns of $\sim$50 μm size with both continuous and dashed lines can be accurately fabricated at a high (averaged) line speed of 4.5 mm s^{-1}. Therefore, the experimental results demonstrated that by using the proposed approach, precision position control can be achieved in high-speed large-range multi-axes nanofabrication.

Acknowledgments

Zou would like to acknowledge the financial support from NSF Grants CMMI 0626417 and DUE 0632908.

References

[1] Curson N J, Nemutudi R, Appleyard N J, Pepper M, Ritchie D A and Jones G A C 1995 Ballistic transport in a GaAs/AlxGa1CxAs one-dimensional channel fabricated using an atomic force microscope *Microelectron* **31** 1244–5

[2] Magno R and Bennett B R 1997 Nanostructure patterns written in III–V semiconductors by an atomic force microscope *Appl. Phys. Lett.* **70** 1855

[3] Michler J, Gassilloud R, Gasser P, Santinacci L and Schmukib P 2004 Defect-free AFM scratching at the Si/SiO$_2$ interface used for selective electrodeposition of nanowires *Electrochem. Solid-State Lett.* **7** A41–3

[4] Piner R D, Zhu J, Xu F, Hong S and Mirkin C A 1999 Dip-pen nanolithography *Science* **283** 661–3

[5] Vettiger P *et al* 2002 The millipede-nanotechnology entering data storage *IEEE* **1** 39–55

[6] Wu Y and Zou Q 2007 Iterative control approach to compensate for the hysteresis and the vibrational dynamics effects of piezo actuators *IEEE Trans. Control Syst. Technol.* **15** 936–44

[7] Kim K S and Zou Q 2008 Model-less inversion-based iterative control for output tracking: piezoelectric actuator example *ACC (Seattle, WA, 2008)*

[8] Tseng A A, Notargiacomo A and Chen T P 2005 Nanofabrication by scanning probe microscope lithography: a review *J. Vac. Sci. Technol.* B **23** 877–94

[9] Chimmalgi A, Grigoropoulos C P and Komvopoulos K 2005 Surface nanostructuring by nano-/femtosecond laser-assisted scanning force microscopy *Appl. Phys.* **97** 104319

[10] Tien S, Zou Q and Devasia S 2005 Iterative control of dynamics-coupling-caused errors in piezoscanners during high-speed AFM operation *IEEE Trans. Control Syst. Technol.* **13** 921–31

[11] Kim K-S, Zou Q and Su C 2008 A new approach to scan-trajectory design and track: AFM force measurement example *ASME J. Dyn. Syst. Meas. Control* **130** 051005

[12] Zou Q and Devasia S 2004 Preview-based optimal inversion for output tracking: application to scanning tunneling microscopy *IEEE Trans. Control Syst. Technol.* **12** 375–86

[13] Xu Z, Kim K-S, Zou Q and Shrotriya P 2008 Broadband measurement of rate-dependent viscoelasticity at nanoscale

using scanning probe microscope: poly(dimethylsiloxane) example *Appl. Phys. Lett.* **93** 133103

[14] Sebastian A and Salapaka S M 2005 Design methodologies for robust nano-positioning *IEEE Trans. Control Syst. Technol.* **13** 868–76

[15] Waite T C, Zou Q and Kelkar A 2008 Inversion-based feedforward approach to broadband acoustic noise reduction *J. Vib. Acoust.* **130** 051010

[16] Shegaonkar A C and Salapaka S M 2007 Feedback based simultaneous correction of imaging artifacts due to geometrical and mechanical cross-talk and tip–sample stick in atomic force microscopy *Rev. Sci. Instrum.* **78** 103706

[17] Hoffmann Ä, Jungk T and Soergel E 2007 Cross-talk correction in atomic force microscopy *Rev. Sci. Instrum.* **78** 016101

[18] Pao L Y, Butterworth J A and Abramovitch D Y 2007 Combined feedforward/feedback control of atomic force microscopes *ACC (New York, 2007)* pp 3509–15

[19] Fang T-H and Chang W-J 2003 Effects of AFM-based nanomachining process on aluminum surface *J. Phys. Chem. Solids* **64** 913–8

[20] Notargiacomo A, Foglietti V, Cianci E, Capellini G, Adami M F, Evangelisti P and Nicolin C 1999 Atomic force microscopy lithography as a nanodevice development technique *Nanotechnology* **10** 458